Comparison of K$_{0.5}$Na$_{0.5}$NbO$_3$ and PbZr$_{0.52}$Ti$_{0.48}$O$_3$ compliant-mechanism-design energy harvesters

Veronika Kovacova, Jung In Yang, Leonard Jacques, Hong Goo Yeo, Valentin Lanari, Christopher Rahn, and Susan Trolier-McKinstry
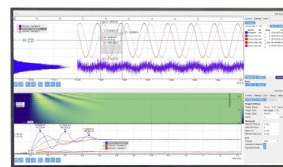
View Online   Export Citation   CrossMark

Comparison of $K_{0.5}Na_{0.5}NbO_3$ and $PbZr_{0.52}Ti_{0.48}O_3$ compliant-mechanism-design energy harvesters

Veronika Kovacova,[1,a)] [ID] Jung In Yang,[1] Leonard Jacques,[1] [ID] Hong Goo Yeo,[2] [ID] Valentin Lanari,[3] Christopher Rahn,[3] and Susan Trolier-McKinstry[1] [ID]

AFFILIATIONS

[1]Materials Science and Engineering Department and Materials Research Institute, The Pennsylvania State University, University Park, Pennsylvania 16802, USA
[2]Department of Advanced Material Engineering, Sunmoon University, Asan, Chungcheongnam-do 31460, South Korea
[3]Mechanical Engineering Department and Materials Research Institute, The Pennsylvania State University, University Park, Pennsylvania 16802, USA

a)Author to whom correspondence should be addressed: veronika@kovacova.fr

ABSTRACT

Piezoelectric energy harvesting from ambient vibrations offers an environmentally friendly approach to powering distributed sensors for the Internet of Things. This paper gives a direct comparison of $Pb(Zr,Ti)O_3$ (PZT)- and $(K,Na)NbO_3$ (KNN)-based harvesters using a compliant mechanism harvester design for resonant frequencies of 20, 40, and 70 Hz. At 70 Hz, the measured power densities for PZT- and KNN-based devices are 1139 and $31\,\mu W/mm^3$, respectively, for unimorph structures on nickel foils of 25 and $50\,\mu m$ in thickness. The power density ratios scale proportionally to the material energy harvesting figures of merit. Energy harvesting with the compliant mechanism design is twice as efficient when compared to harvesting with a simple cantilever beam.

Published under license by AIP Publishing. https://doi.org/10.1063/5.0037731

I. INTRODUCTION

The increasing number of interconnected objects constituting the Internet of Things (IoT) needs to be powered to function.[1] Periodic battery changes for widely distributed networks of sensors are challenging; therefore, more sustainable approaches using alternative energy sources are of interest. Wind and solar power are intermittent and are not available in all locations. In some of these places, however, mechanical energy from ambient vibrations is predictable and available.[2] For example, heating, ventilation and air-conditioning (HVAC) vents in office buildings resonate at 60 Hz with peak accelerations from 0.2 to 1.5 m/s^2.[3] These mechanical vibrations can be transformed into electrical energy with high-power density harvesters using the direct piezoelectric effect.

Many groups have investigated piezoelectric harvesting of electrical power from vibrations at different frequency ranges, at different scales from MEMS to macroscopic beams, with resonant or non-resonant structures, with various geometries from simple cantilever beams to more complex structures enabling more uniform strain distribution with lead-based and lead-free active materials.[4–24]

The highest output power range is achieved using PZT-based ceramics.[4,5] Bulk ceramic active materials have large thicknesses and, therefore, large bending stiffness, which results in high resonant frequencies. Due to their brittle character, ceramics do not withstand large strains. In order to design a harvester for low resonant frequencies, a long beam length, large proof mass, or low bending stiffness of the beam is required. The bending stiffness is proportional to the area moment of inertia and the materials Young's modulus. Thus, for low frequency harvesting, small structures made of micromachined structures on silicon, thin flexible substrates, such as metallic films, or low stiffness substrates, such as Mylar, are of interest. Jeon *et al.* worked on a microelectromechanical system (MEMS) energy harvester device using the PZT film with d_{33} mode harvesting providing power of $1\,\mu W$ at 13.9 kHz.[6] Shen *et al.* also reported an MEMS-based harvester; however, they achieved lower resonant frequency. The output power of the harvester was $0.34\,\mu W$ at 183.8 Hz under 0.75 G (G = 9.81 m/s^2).[7] Won *et al.* utilized a small beam cross section (a stress-engineered $1\,\mu m$ thick PZT thin film on a

25 μm-thin Ni–Cr based austenitic steel metal foil) in a small-scale harvester without any complex MEMS or etching. This device provided 5.6 μW with a peak voltage of 690 mV at 127 Hz under 0.5 G acceleration (G = 9.81 m/s^2).[8] More recently, Godard et al. used the approach of low stiffness polymer substrate to decrease the resonant frequency. The active material was multi-layered screen-printed P(VDF-TrFE). Their transducer was able to harvest 0.97 mW at 33 Hz under a large acceleration of 5.8 G.[9]

More efficient transducer designs can increase the power output of piezoelectric harvesters. This entails ensuring that the piezoelectric material is effectively strained up to the maximum strain tolerated by the piezoelectric material. PZT thin films on nickel substrates withstand strain levels up to 0.5% depending on the thickness and microstructure,[10] whereas PVDF films on Mylar are able to withstand strains up to 1%–2%.[9] The strain homogeneity plays a crucial role in the amount of power generated. The strain distribution in a simple cantilever beam decreases linearly from the clamped end toward the beam tip, where it is close to zero. Therefore, the root of the cantilever generates more power than the portion close to the beam tip. Thus, a simple cantilever beam produces only 20%–24% of the power that would be generated if an equivalent volume of piezoelectric material was strained uniformly throughout its length.[8] Designs that make the strain distribution within the piezoelectric material both uniform and comparatively high are more efficient.[11–13] Yeo et al. developed piezoelectric energy harvesters that combined a high performance Mn doped Pb(Zr,Ti)O$_3$ (Mn-PZT) 3 μm active layer deposited on 25 μm nickel foil[14] with the 65% mode shape efficiency of the compliant mechanism design proposed by Ma et al.[11] The reported output power at 6 Hz under 0.05 G was 50 μW. This corresponds to an energy density as high as 9.75 μW/cm^2.[14]

oGiven the potential widespread distribution of mechanical energy harvesters in the environment for powering IoT applications and new legislation limiting lead usage due to its high neurotoxicity,[15–17] there is a need for developing high-quality and competitive lead-free piezoelectric layers. Moreover, high output power piezoelectric lead-free materials could open new possibilities for medical applications due to better biocompatibility.[18,19] Poly(vinylidene fluoride)-based (PVDF) piezoelectric polymers are interesting because they are lead-free, compatible with a variety of possible substrates, and widely commercially available; however, their main drawbacks are low power density and difficulty in impedance matching. On the other hand, lead-free ceramics show higher power densities. Biocompatibility and high-power density are necessary for applications such as implantable energy harvesters.[20]

(K,Na)NbO$_3$ (KNN) is one of the most promising lead-free ceramic with a PZT-competitive piezoelectric coefficient, high-power density, and biocompatibility.[21–26] Although KNN is a suitable candidate, it often has higher leakage currents[27] due to hygroscopic secondary phases originating from nonstoichiometry related to alkali loss during deposition.[28] Leakage currents can be optimized by adjusting deposition conditions, alkali excess, or doping.[27,29,30] Zheng et al. reported that a 1 mol. % Mn doped bulk KNN integrated into a cantilever beam resonating at 90 Hz harvested 16 μW at 1 G acceleration. The corresponding volume power density was 0.32 μW/mm^3.[31] Thin film KNN has also been used for energy harvesting. Mn doped sol–gel deposited (100) oriented KNN is reported to exhibit an $e_{31,f}$ equal to -8.5 C/m^2. With a relative permittivity (ϵ_r) of 788, this film shows a figure of merit $\left(\text{FoM} = \frac{e_{31,f}^2}{\varepsilon_r} \right)$ as high as 0.09 C^2/m^4.[32] Kanno et al. used a sputter deposited KNN integrated into a harvester resonating at 1036 Hz, which generated 1.1 μW at 1G. The corresponding power density was 6.5 μW/mm^3.[33] Won et al. reported a KNN MEMS energy harvester that resonated at 132 Hz; under an acceleration of 1 G, it produced 3.62 μW of power with a peak voltage of 520 mV.[32] In 2015, Kim et al. designed harvesters utilizing a KNN film deposited on the Si substrate and transferred to a flexible polyimide substrate, which resonated at low frequencies from 3 to 15 Hz. Such harvesters provided a maximum power of 0.076 μW, corresponding to 2.9 μW/mm^3.[34] Tsujiura et al. reported an energy harvester based on 2.2 μm thick KNN deposited on austenitic stainless steel SS304. The harvester has a cantilever beam geometry, operates at 393 Hz and delivers 130 mV and 3.2 μW of maximum power under an acceleration of 10 m/s^2. The corresponding power density is 38.7 μW/mm^3. A summary of energy harvesters using KNN active layers is given in Table I.

The aim of this study is to design efficient harvesters using the compliant mechanism design with resonance frequencies under 100 Hz using lead-based and lead-free piezoelectric layers. This was approached by designing efficient compliant mechanism harvesters with resonant frequencies of 20, 40, and 70 Hz. Important parameters that insure the quasi-quadratic mode shape are discussed. Both lead-based and lead-free piezoelectric active layers are integrated into the harvesters, and their voltage and power output are measured for the same resonant frequencies. The resulting harvester performance and efficiency are discussed.

TABLE I. KNN-based energy harvesters.

Material	Form	Frequency (Hz)	Voltage (V)	Power (μW)	Power density (μW/mm^3)	Reference
1% Mn KNN	Bulk	90	7	16	0.32	Zheng et al.[31]
KNN	3 μm film	1036	0.1	1.1	6.5	Kanno et al.[33]
0.5% Mn KNN	1 μm film	132	0.5	3.6	1.8	Won et al.[32]
KNN	310 nm film	3–15	1.9	0.076	2.9	Kim et al.[34]
KNN	2.2 μm film	393	0.13	3.2	38.7	Tsujiura et al.[35]

II. EXPERIMENTAL PROCEDURE

Piezoelectric films were deposited on 25 and $50\,\mu$m thick 99.9% pure nickel foil substrates purchased from Sigma Aldrich and 99.98% foil from Hpulcas. Prior to deposition, the Ni foils were manually polished using alumina powders of 3, 1, 0.3, and $0.05\,\mu$m average particle sizes, successively. The foils were ultrasonically cleaned with DI water and isopropanol between each polishing step. The foils were then annealed at 900 °C for 1 h in an N_2/H_2 reducing conditions at atmospheric pressure to eliminate NiO. The gas settings were 136 sccm of wet nitrogen, 354 sccm of dry nitrogen, and 200 sccm of a mixture of 5% hydrogen/95% nitrogen. Then, 30 nm of HfO_2 was deposited on both sides of the foils using atomic layer deposition with the ALD System 150LE tool from Kurt J. Lesker. Deposition was performed at 200 °C using water as the oxidant.

$LaNiO_3$ (LNO) bottom electrodes were then sputtered from an LNO ceramic target in a Lesker CMS-18 tool to facilitate preparation of [100] oriented piezoelectric layers such as $Pb(Zr,Ti)O_3$.[14] Deposition was performed under 31.4 sccm of argon and 10.4 sccm of oxygen at a chamber pressure of 12 mTorr, a target power of 90 W, and a substrate temperature of 275 °C. The LNO bottom electrode for the PZT sample was deposited by a sol–gel method. 0.2M LNO chemical solutions based on lanthanum (III) nitrate hexahydrate and nickel (II) acetate tetrahydrate precursors and 2-methoxyethanol (2MOE) solvent were spin coated on one side of the Ni foil at a time and pyrolyzed on a hot plate in air. Each $LaNiO_3$ layer was crystallized in rapid thermal annealing furnace for 1 min at 700 °C in air; these processes were repeated five times to fabricate a 100 nm-thick [100]-oriented LNO layer.

The 1 mol. % Mn doped PZT solution preparation and the unimorph $1\,\mu$m thick film deposition process on $25\,\mu$m thick nickel foil are similar to that described elsewhere.[36] 0.5 mol. % Mn doped $K_{0.5}Na_{0.5}NbO_3$ (KNN) thin films were prepared by the sol–gel chemical solution deposition (CSD) method with solution synthesis according to route A, as described in Kovacova et al.[30] The precursor solutions were spun on Ni foils at 3000 rpm for 30 s. After spinning, the samples were dried at 200 °C for 2 min and pyrolyzed at 300 °C for 3 min on hot plates. All samples were crystallized at 750 °C for 5 min in air in a rapid thermal annealing (RTA) furnace. The deposition steps were repeated until the desired thickness of $1\,\mu$m was achieved.

The resulting films were characterized for their structure and microstructure. High-resolution micrographs of the surface and cross section of the PZT and KNN films were obtained using field emission scanning electron microscopy (Zeiss Merlin) at a 5 kV accelerating voltage. X-ray diffraction patterns for each film were collected with either an Empyrean PANalytical laboratory diffractometer or a Malvern Panalytical XPert Pro MPD in Bragg-Brentano geometry. The 2θ range was set from 10° to 70°.

A lift off procedure was used to pattern top electrodes for electrical measurements. LOR 5 and SPR 2013 positive photoresists were spun onto the sample surfaces and patterned by contact photolithography; features were patterned with diameters of 200, 400, 600, and $1000\,\mu$m for $e_{31,f}$ direct piezoelectric coefficient measurements and $3 \times 6\,mm^2$ and $2 \times 4\,mm^2$ for energy harvesters. A 100 nm-thick Pt layer was deposited by RF sputtering in Kurt
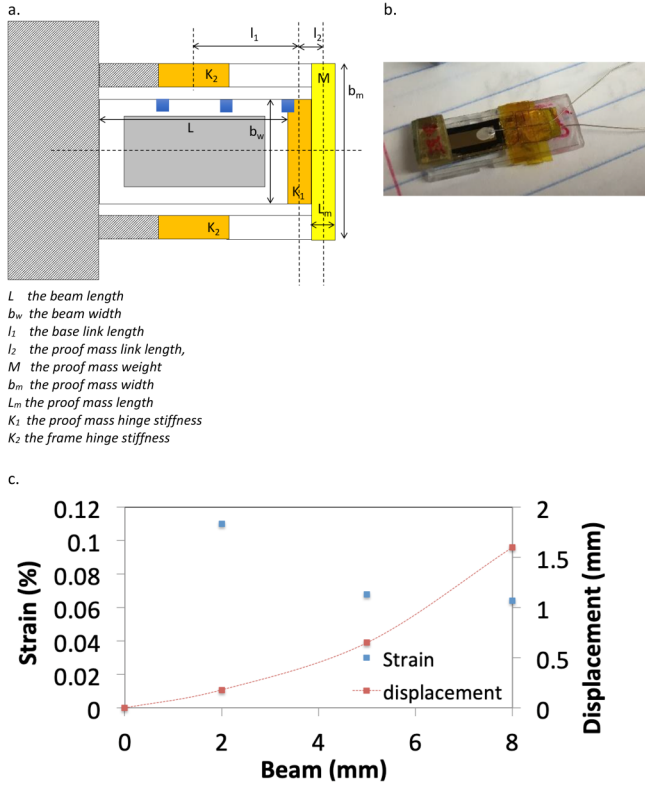
Lesker CMS-18 sputtering tool. After a standard lift off process, Pt top electrodes were post-annealed in RTA at 500 °C for 1 min in air to improve the interface adhesion between the Pt electrodes and the PZT and KNN films.

Electrical measurements were made to assess the low and high field dielectric responses of the films. The films' relative permittivity and dielectric loss were measured using an LCR meter (Hewlett Packard 4284A, Palo Alto, USA) from 50 Hz to 500 kHz with a 30 mV AC signal. A Multiferroic Test System (Radiant Technology, Inc., Albuquerque, NM) was used to perform high field measurements of polarization vs electric field hysteresis loops (P-E loop) at 1 kHz and 400 kV/cm.

The $e_{31,f}$ piezoelectric coefficient was measured using an in-house wafer flexure tool.[37] For this purpose, Ni foils with piezoelectric films were superglued onto a 6-in. silicon carrier wafer. Then, strain gauges were glued on top of the samples. Before measurements were taken, electrodes were poled at three times the coercive field at 150 °C for PZT as described elsewhere.[36] KNN samples were poled at temperatures ranging from RT up to 150 °C. Initial $e_{31,f}$ enabled to find optimum poling conditions for energy harvesting measurements. The best values were at three times the coercive field at 85 °C. Samples were strained at $5.23\,\mu$-strains at 4 Hz to obtain the $e_{31,f}$ coefficients.

Piezoelectric films with large electrodes were integrated into harvesters using the compliant mechanism design described by Ma et al..[11,38] The compliant design consists of a piezoelectric beam, a fixed frame, and a moving frame carrying the seismic mass [see Fig. 1(a)]. The fixed and moving parts of the frame attach with the K hinges; the beam attaches to the moving part of the frame with the K_1 hinge. As reported elsewhere, the K_1 hinge stiffness is responsible for enabling a uniform strain distribution in the piezoelectric layer.[11] The frame is laser cut from 1.5 mm-thin acrylic plates, the K_2 hinge is made of Mylar, and the K_1 hinge is fabricated with Kapton tape layers. In order to dimension the harvester for a particular resonant frequency, the equivalent mass and subsequently the proof mass value have to be determined. Harvester frames with proof masses were dimensioned in order to obtain resonant frequencies of 20, 40, and 70 Hz. A shaker table (F3, Wilcoxon) was used as a vibration source. The sinusoidal excitation frequency and base excitation level were controlled using a lock-in-amplifier (SRS830, Stanford Research Systems). An accelerometer (352C65, PCB Piezotronics) with a sensitivity of 100 mV per G was mounted on the shaker to verify the vibration frequency and measure acceleration level. A resistor box was used to alter the load resistance to determine the optimum value showing maximum output power. During vibration of the shaker, the mechanical input (operating frequency and excitation level) and the output voltage developed by the harvester were monitored on an oscilloscope (TDS3054C, Tektronix).

Laser vibrometer measurements were performed for two reasons. First, the K_1 hinge stiffness connecting the beam and the moving part of the frame of the harvester must be optimized in order to achieve good strain homogeneity across the beam length. For this purpose, displacement values were measured at different points on the beam. Second, laser measurements determined the maximum acceleration allowed to avoid exceeding the strain limit of the material. The energy harvester design in this work has a

- L the beam length
- b_w the beam width
- l_1 the base link length
- l_2 the proof mass link length
- M the proof mass weight
- b_m the proof mass width
- L_m the proof mass length
- K_1 the proof mass hinge stiffness
- K_2 the frame hinge stiffness

FIG. 1. Schematic (a) and image (b) of the harvester dimensioned for a resonance frequency of 40 Hz. Blue squares on the schematic represent reflective tape positions for displacement measurements. The beam displacement and strain values at three positions on the beam (c) under acceleration of 0.93 G with five layers of tape for K_1 hinge stiffness.

mechanical quality factor exceeding 5, which means that its lifetime is limited by mechanical failure.[39] In order to ensure mechanical resistance to fatigue of the piezoelectric beam, a safety factor k is used to determine the tensile strain limit S_{lim} from the breakdown strain S_b,

$$S_{lim} = \frac{S_b}{k}. \tag{1}$$

Coleman *et al.* recently reported tensile and compressive strain boundaries for the PZT film on Ni foils above which mechanical failure occurs. The breakdown tensile strain was 0.5%.[10] For this work, the safety factor was set to 5, resulting in the maximum allowed strain equal to 0.1%. Since the strain is largest at the beam clamping point, the acceleration was adjusted to attain 0.1% strain in that region.

III. DIMENSIONING PROCESS

The beam dimensions were chosen based on the electrode size available for KNN films. Since KNN has a higher leakage current

density than PZT, different electrode sizes were utilized for harvesting. After initial testing, electrode sizes of $3 \times 6\,mm^2$ and $2 \times 4\,mm^2$ were chosen. The beam size was set to $4.5 \times 8\,mm^2$ for all beams. The L_1 link length was set to 4.5 mm.

PZT and KNN films were deposited on buffered 25-μm thick nickel foils. KNN, however, developed surface features of 50-μm size resulting from the substrate deformation with an increasing number of annealing steps at 750 °C, as shown in Fig. 2 of the supplementary material. Therefore, KNN was also deposited on 50-μm thick foils, resulting in a better surface quality.

The resonance frequencies were set to 20, 40, and 70 Hz for 25-μm thick foils and 40 and 70 Hz for 50-μm thick nickel foils. The K_1 hinge stiffness, the equivalent mass M_{eq}, and seismic mass values M were calculated using[11]

$$K_1 = \frac{\sqrt{2}l_1 b^2 \sqrt{(c_s I \omega)^2 + EI^2}|\sigma_1|}{|(1+j)\sigma_2 - 2l_1 b(j + e^{2Lb} - e^{j2Lb} - je^{2(1+j)Lb})|}, \tag{2}$$

$$M_{eq} = \frac{\left|\sqrt{2}l_1 b^2 \sqrt{(c_s I \omega)^2 + EI^2}|\sigma_1| + (1+1)K_2\sigma_2\right|}{\sqrt{2}\omega^2 l_1^2 |\sigma_2|}, \tag{3}$$

$$b = \sqrt[4]{\frac{m\omega^2}{EI}}, \tag{4}$$

$$\sigma_1 = (e^{Lb} + e^{jLb})^2 + (1 + e^{(1+j)Lb})^2, \tag{5}$$

$$\sigma_2 = (e^{Lb} + e^{jLb})^2 - (1 + e^{(1+j)Lb})^2, \tag{6}$$

$$M_{eq} = M\left(\frac{l_1 + l_2}{l_1}\right)^2 + J\left(\frac{1}{l_1}\right)^2. \tag{7}$$

Note that l_1 stands for the base link length, c_s is the strain rate damping coefficient, I is the equivalent area moment of inertia, EI is the bending stiffness, ω is the resonant frequency, L is the beam length, l_2 is the proof mass link length, m is the beam mass, and J is the rotary inertia. For calculations, the value of L_2 link length was 1.5 mm, and K_2 was set to 0 as it would be in ideal conditions.

Resonance frequencies were verified with the characteristic Eq. (8) of the compliant system,[27]

$$
\begin{aligned}
&-\frac{K_2 L}{EI}(1 - \cos\lambda\sin\lambda) + \lambda\frac{K_1 + K_2}{K_1}(\cos\lambda\sinh\lambda - \sin\lambda\cosh\lambda) \\
&+ \lambda^2\frac{2l_1}{L}\sin\lambda\sinh\lambda - \lambda^3\frac{l_1^2}{L^2}(\cos\lambda\sinh\lambda + \sin\lambda\cosh\lambda) \\
&+ \lambda^4\left[\frac{M_{eq}l_1^3}{mL^3}(1 - \cos\lambda\cosh\lambda) - \frac{EIl_1^2}{K_1 L^3}(1 + \cos\lambda\cosh\lambda)\right] \\
&\times \lambda^5\frac{M_{eq}EIl_1^2}{mK_1 L^4}(\cos\lambda\sinh\lambda - \sin\lambda\cosh\lambda) = 0, \tag{8}
\end{aligned}
$$

where λ_r are the eigenvalues of the system. λ_r are related to the resonant frequencies ω_r as follows:

TABLE II. Equivalent masses, K_1 hinge stiffness, and seismic masses for transducers as a function of beam thicknesses and targeted resonance frequencies.

Beam thickness (μm)	25			50	
Resonance frequencies (Hz)	20	40	70	40	70
Equivalent masses (g)	0.536	0.132	0.041	1.059	0.343
K_1 hinge stiffness (N m/rad)	0.001 38	0.001 42	0.001 51	0.010 9	0.011 1
Seismic masses (g)	0.282	0.079	0.022	0.548	0.185

$$\lambda_r = L \sqrt[4]{\frac{m\omega_r^2}{EI}}. \tag{9}$$

The first mode resonant frequency is determined from λ_1 and corresponds to ω_1.

Table II summarizes the transducer dimensions. All harvesters had the same dimensions, as shown in Fig. 1(a). The dimensions of the harvester with a 25-μm thick substrate and resonating at 40 Hz are shown in Fig. 1(b).

The calculated values of the K_1 hinge stiffness were used as a starting point. Two approaches were then explored to experimentally adjust the hinge stiffness. First, the hinges were adjusted by adding layers of Kapton tape to achieve a quadratic mode shape. This was done by monitoring the voltage output as a function of the number of Kapton layers utilized as the maximum voltage for a given acceleration level is achieved when the strain distribution is uniform. However, this approach does not produce quantitative information on either the strain distribution or the maximum strain values as a function of acceleration. Therefore, a second approach was adopted by measuring displacement at different points along the beam with a laser vibrometer and calculating the corresponding strain levels using Euler–Bernoulli beam theory, as shown in Fig. 1(a). The points measured along the beam are represented as blue squares in Fig. 1(a). The stiffness of the K_1 hinge was chosen to minimize the strain variation along the beam and it was calculated from experimental values of displacement. The acceleration level of the shaker was adjusted carefully so as to not exceed a maximum strain of 0.1% at 2 mm from the beam clamp. Figure 1(c) shows the beam deflection profile (red curve) and the strain distribution (blue boxes) along the beam for 25 μm thick beam harvester resonating at 40 Hz. The strain distribution was adjusted via the K_1 hinge stiffness; the maximum strain near the beam clamp was adjusted for the acceleration level. Reflective tape was glued to the beam surface to ensure a high-quality signal from specific locations on the beam surface.

Acceleration is related to the peak displacement and frequency for a sinusoidal motion as

$$A = \frac{2\pi^2 f^2 D}{G}, \tag{10}$$

where A is the acceleration, f is the frequency, D is the maximum displacement, and G is the acceleration of gravity. Thus, to achieve the same beam displacement and the same strain level, the acceleration needs to increase to the power two with frequency. Table III

summarizes the maximum allowed acceleration corresponding to 0.1% strain for harvesters resonating at different frequencies according to these measurements. These values are in good agreement with theory.

IV. PZT AND KNN THIN FILMS

Figure 2 shows cross sections of PZT (a) and KNN (b) layers on Ni foils. The microstructure of both films is dense and columnar. Surface micrographs of the PZT and KNN thin films are shown, respectively, in Figs. 1(a) and 1(b) of the supplementary material. The grain sizes of the PZT and KNN films are 110 ± 45 and 228 ± 74 nm, respectively. It was found that KNN on the 25 μm thick Ni foil shows enhanced surface buckling after repeated RTA at 750 °C. A representative field emission scanning electron microscope (FESEM) image is shown in Fig. 2 of the supplementary material. In contrast, KNN deposited on the 50 μm thick Ni foil resulted in a better surface quality.

The XRD pattern of the {100} oriented PZT is shown elsewhere.[36] The XRD pattern for the KNN film is shown in Fig. 3 of the supplementary material. KNN films are polycrystalline with a {100} Lotgering factor of 0.42 and 0.18 for KNN deposited on 25 and 50 μm thick nickel foils, respectively, using PDF file 01-085-2526[40] and the integrated areas of KNN diffraction peaks fitted using the Pseudo-Voigt function.

Figure 3 shows the dielectric properties of KNN and PZT deposited on the Ni foil. At 50 Hz, the relative permittivity of KNN and PZT is 630 and 390, respectively. The dielectric loss of KNN and PZT are 5% and 2%, respectively. The remanent polarization of KNN was 18 μC/cm^2, and the coercive field was 97 kV/cm (Fig. 4 in the supplementary material). The remanent polarization of PZT was 38 μC/cm^2, and the coercive field was 50 kV/cm.[36]

Measurements of the direct piezoelectric coefficient $e_{31,f}$ were performed on poled PZT and KNN. $e_{31,f}$ was equal to -12.0 and -2.6 C/m^2, respectively, for PZT and KNN. The energy harvesting FoM was, thus, 0.37 and 0.01 C^2/m^4 for these PZT and KNN films, respectively.

TABLE III. Acceleration levels as function of beam thicknesses and resonant frequencies.

Beam thickness (μm)	25			50	
Resonance frequencies (Hz)	20	40	70	40	70
Theoretical acceleration (G)	0.2	0.8	2.45	0.36	1.1
Experimental acceleration (G)	0.3	0.9	2.5	0.4	1.5
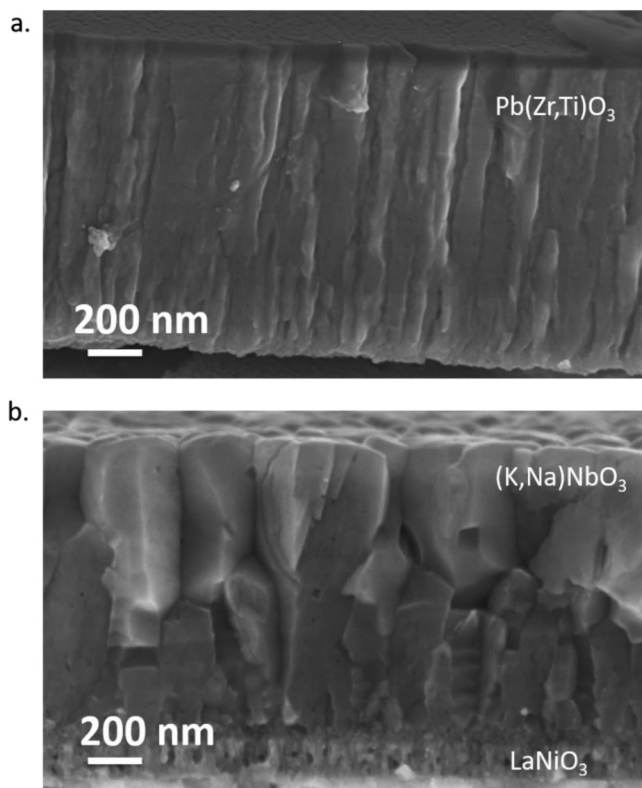
FIG. 2. FESEM images of the cross section of PZT (a) and KNN (b) deposited on Ni foils.

FIG. 3. Relative permittivity and dielectric loss of KNN and PZT films.

V. POWER MEASUREMENTS

The piezoelectric beams were then integrated into compliant design harvesters dimensioned for resonance frequencies of 20, 40, and 70 Hz. Figure 4 shows peak-to-peak voltage and maximum power output for harvesters using PZT layers. The actual measured resonance frequencies of the harvesters were 23, 42, and 70 Hz. The discrepancies between dimensioned and measured resonance frequencies are likely due to differences in assembly steps or in harvester clamping conditions. The surface area of electrodes was $3 \times 6 \, \text{mm}^2$. The maximum peak-to-peak voltage was between 1.9 and 2.2 V, and the maximum power output after impedance matching was 4.8, 13, and 20.5 μW for 23, 42, and 70 Hz resonating harvesters, respectively. An example of the frequency and acceleration sweep for a 42 Hz resonating harvester is shown in Fig. 5 in the supplementary material. The mechanical quality factor of the device was 12.1, and the mechanical damping was equal to 4.1%. For harvesters having a mechanical quality factor larger than 5, the mechanical fatigue and strain limitations dominate the power density. Precautions such as the safety factor were taken in order to prevent mechanical failure.[39]

Power outputs from harvesting can be converted into areal power densities by dividing the output power with the electrode surface area. Corresponding areal power densities for PZT-based harvesters are 26.7, 72.2, and 113.9 μW/cm^2 for 23, 42, and 70 Hz, respectively. In practice, this means that a unimorph harvester with 1 cm^2 of 1 μm thick PZT active layer would provide 113.9 μW of power at 70 Hz. In terms of volume power density, PZT-based harvesters produce 267, 722, and 1139 μW/mm^3 for 23, 42, and 70 Hz, respectively.

A harvester with a $3 \times 6 \, \text{mm}^2$ KNN electrode on the 25-μm thick Ni foil substrate resonating at 40 Hz was measured. The peak-to-peak voltage was 230 mV, the maximum output power of the harvester was 0.2 μW, and the corresponding areal power output density was equal to 1.1 μW/cm^2. These values are shown in Fig. 6 in the supplementary material. A one to one comparison of 1 μm thick PZT and KNN piezoelectric layer deposited on the 25-μm thick Ni foil with the same active areas resonating at 42 and 40 Hz under the same acceleration show that PZT produces 9 times more voltage and 65 times more power. The PZT and KNN power output ratio is nearly twice as large as the ratio of FoM corresponding to PZT and KNN, which is equal to 33.6. This suggests that besides the material itself, there is another phenomenon that decreases the power output of KNN. Figure 2 in the supplementary material shows buckling with a characteristic 50-μm dimension on the surface of KNN film deposited on a 25 μm thick Ni substrate. Note that the dimensions of these patterns correspond to the size of nickel grains. It can be hypothesized that such patterns cause local strain level fluctuations leading to underperformance in KNN-based harvesters.

The power outputs of harvesters with KNN deposited on 50-μm thick Ni foils were measured to verify if the power difference was due to the material or due to the surface buckling of KNN on a 25-μm Ni foil. Figure 5 shows the peak-to-peak voltage and the maximum power output for harvesters with 1 μm thick KNN with active are of $2 \times 4 \, \text{mm}^2$ on 50 μm Ni foils integrated into compliant mechanism harvesters resonating at 40 and 70 Hz under 0.1% strain adjusted using a laser vibrometer. The maximum peak-to-peak voltages for 40 and 70 Hz are 350 and 375 mV, respectively. The maximum powers at optimal load resistance for 40 and 70 Hz are
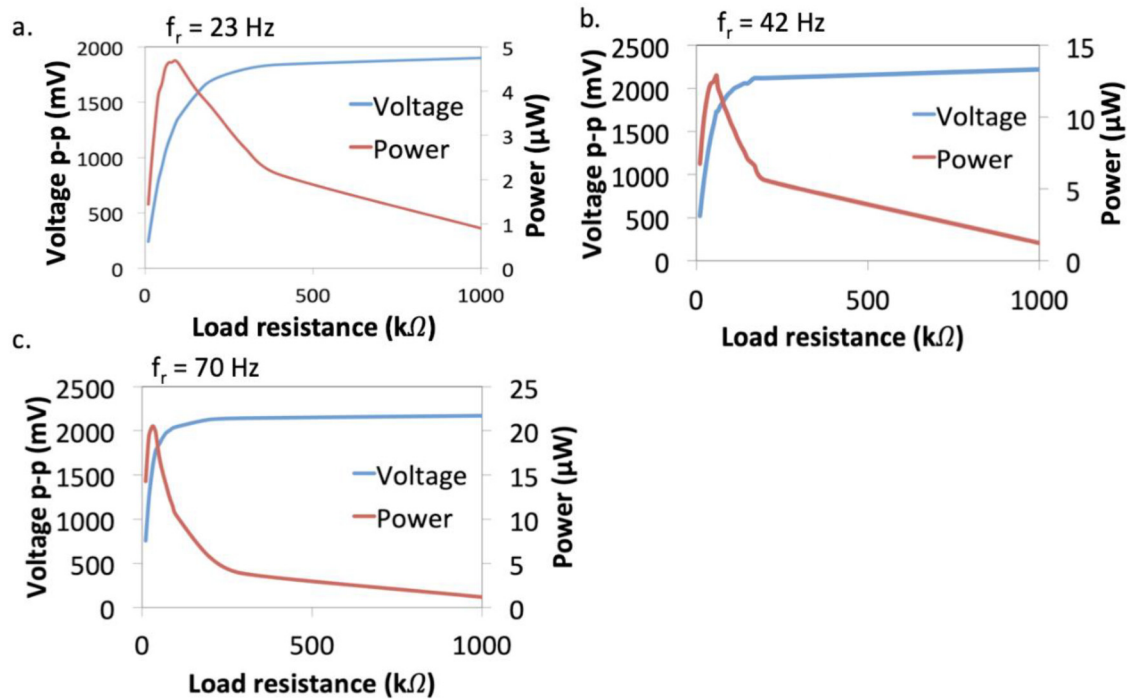
FIG. 4. Peak-to-peak voltage and maximum power for PZT-based energy harvesters with the 25 μm thick Ni foil substrate at 23 (a), 42 (b), and 70 Hz (c).

0.15 and 0.25 μW, respectively. The corresponding areal power densities are 1.9 and 3.1 μW/cm^2, and volume power densities are 19 and 31 μW/mm^3, respectively. In order to produce 100 μW of output power, a 3-μm thick bimorph KNN beam with an active area of 5.4 cm^2 on both sides would be needed.

An example of a frequency sweep of the harvester with KNN on 50 μm Ni foils resonating at 40 Hz is shown in Fig. 7 in the supplementary material. The mechanical quality factor is equal to 9.6, and the mechanical damping is 5.2%.

Table IV compares the areal power density of PZT- and KNN-based harvesters. The ratio of experimental power outputs of PZT and KNN on 50-μm thick substrate is 38.5 and 36.4 for 40 and 70 Hz, respectively. These values are close to the theoretical value of the ratio of FoM for PZT and KNN, which is 33.6. This result confirms the hypothesis that surface buckling of the KNN/25 μm thick Ni foil harvesters decreases harvesting performances.

The experimental power density outputs for PZT and KNN were then compared to the theoretical values. Harvesting efficiency is defined as the ratio between theoretical and experimental power outputs. The theoretical power output was calculated for PZT and KNN harvesters using

$$P_{max, theory} = \frac{(S_{lim}E_p d_{31f})^2 L b_w h_p \omega}{2\varepsilon_{33}^S}, \quad (11)$$

where E_P stands for Young's modulus of the piezoelectric layer, d_{31f} is the effective piezoelectric coefficient, L stands for the beam

length, b_w is the beam width, h_p is the thickness of the piezoelectric layer, ω is the resonant frequency, and ε_{33}^S is the relative permittivity under zero strain.

Figure 6 plots the theoretical and experimental maximum power output for PZT and KNN. Theoretical power is calculated assuming that the whole piezoelectric layer is uniformly strained at 0.1%. From the experimental strain measurements on a PZT-based harvester resonating at 40 Hz [Fig. 1(c)], it is shown that after optimization, the strain level at the beam tip is 58% of the strain level near the beam clamp. Therefore, strain non-uniformity has a direct consequence on the power output. The experimental power output is equal to 48% of the theoretical power output. Note that the efficiency of a simple cantilever beam is only 20.5%. The use of the compliant design increases harvesting efficiency to 48%; these values are smaller than the 64% efficiency values reported by Ma et al.[11] and Yeo et al.[14] for a larger, lower frequency design. The origin of the efficiency difference might be due to the miniaturization of the compliant design used in this study.

The prototypes in this study utilize reasonable quality KNN films integrated into harvesters using the compliant mechanism design that increases the overall efficiency of harvesting. Moreover, the devices are designed for resonant frequencies below 120 Hz, which is the frequency range of interest for the IoT. Indeed, several KNN films reported in the literature show higher FoM; 0.09 C^2/m^4 in Shibata et al.[21] and 0.035 C^2/m^4 in Tsujiura et al.[35] The FoM of the KNN in this work is 0.01 C^2/m^4. The strength of the material here is that on nickel foils, the dielectric losses remain under 6 % at
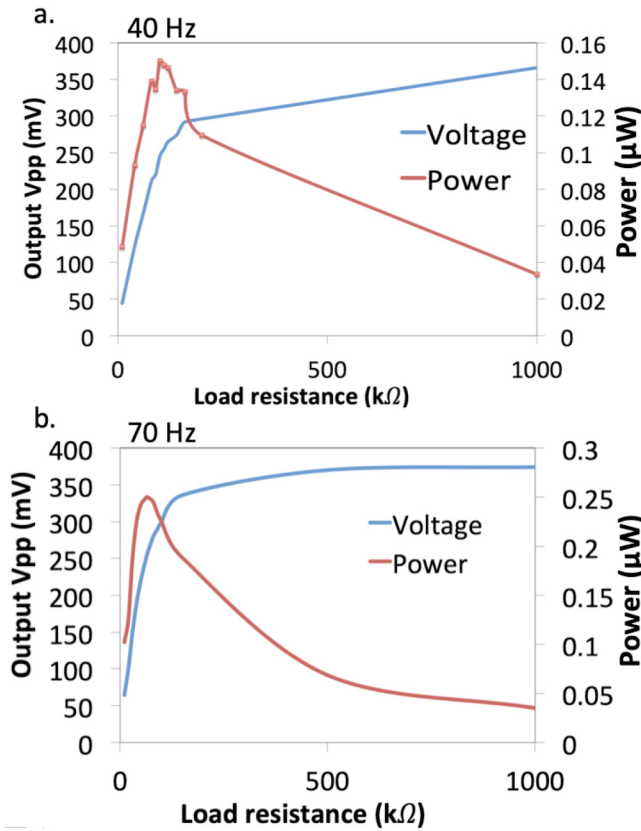
FIG. 5. Peak-to-peak voltage and maximum power for KNN-based energy harvesters with the 50 μm thick Ni foil substrate resonating at 40 and 70 Hz.
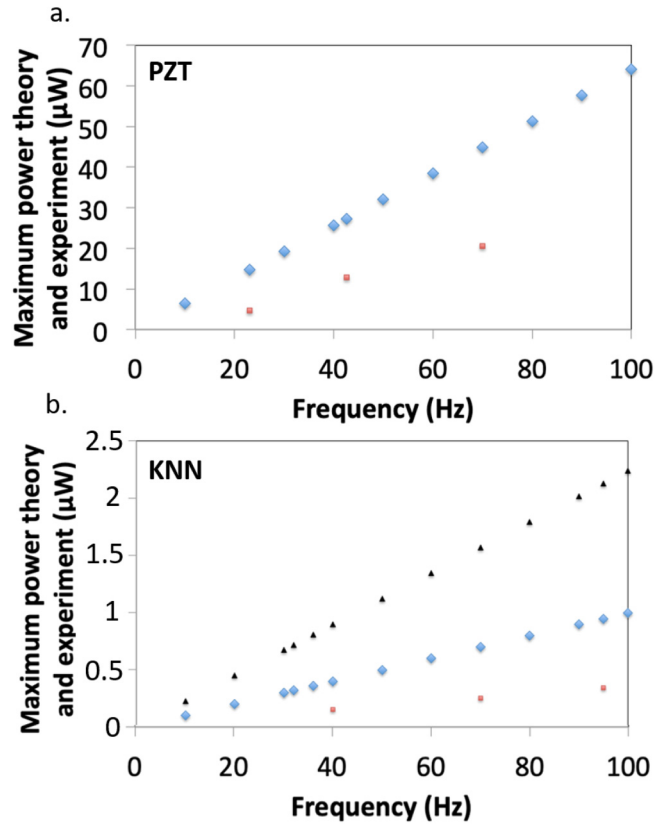

FIG. 6. (a) Theoretical limit (blue) and experimental (red) maximum power output at optimal load resistance for PZT for electrode area of 3×6 mm^2. (b) Theoretical limit (blue) and experimental (red) maximum power output at optimal load resistance for KNN for an electrode area of 2×4 mm^2. Theoretical power limit for KNN for 3×6 mm^2 electrode area for KNN (black).

<120 Hz. In contrast, the KNN integrated on steel reported by Tsujiura *et al.* shows dielectric losses of 56%. High dielectric losses correspond to high charge leakage across the piezoelectric, which is detrimental to the output power. Thus, the KNN films discussed here show the lowest dielectric loss reported of the KNN film integrated on foils.

In addition, these experiments show that the compliant mechanism design increases the output power by a factor of 2.4 in comparison to the simple cantilever beam. This study experimentally confirms the interest of the compliant design harvester for broad frequency range up to 70 Hz.

The average grain size of the PZT film is smaller than the average grain size of the KNN film; however, these values are in the range of typical grain sizes for these materials reported in the literature.[41–44] It has been shown previously that increased grain size in PZT leads to improved dielectric and piezoelectric properties.[42,45] For KNN films, it is often difficult to decouple changes in grain size from changes in leakage at the grain boundaries.[44] The KNN films used in this study were chosen to show low dielectric losses.

The Lotgering factor enables assessment of the texture of crystalline materials. This factor is equal to 1 for perfectly oriented and 0 for randomly oriented materials. It has been previously reported that preferred orientation has a direct impact on the piezoelectric coefficients in PZT and KNN thin films.[46–48] [100]-oriented KNN have been reported to exhibit $e_{31,f}$ in the range from −10 to −14 C/m^2.[21] The KNN film in this study has a Lotgering factor of 0.18 and 0.42 for [100]-orientation, which corresponds to the modest level of preferred orientation. Larger piezoelectric coefficients resulting in larger power outputs are expected in KNN films with Lotgering factors close to 1 for [100]-orientation.

TABLE IV. Maximum experimental areal power output densities for harvesters with PZT and KNN active layers.

Active material	PZT			KNN		
Substrate thickness (μm)		25		25	50	
Resonance frequency (Hz)	23	42	70	40	40	70
Power areal density (μW/cm^2)	26.7	72.2	113.9	1.1	1.9	3.1
Power density (μW/mm^3)	267	722	1139	11	19	31

VI. CONCLUSION

This paper compares harvesters designed for the same resonant frequencies using 1-μm thick PZT and KNN active layers deposited on Ni foil substrates. The compliant design was utilized to enhance efficiency. The maximal harvesting efficiency was 48%, twice as large as that of the simple cantilever beam design. Dimensioning and parameter adjustments responsible for a nearly quadratic mode shape were found to be important in maximizing power output. 1 μm PZT patterned with 3×6 mm^2 electrode, deposited on 25-μm Ni foil provided a volume power density as high as 1139 μW/mm^3 at 70 Hz. In the same strain and frequency conditions, the measured power density of 1 μm KNN was 31 μW/mm^3. The difference in power densities of PZT and KNN was likely due to differences in material performance because the results are proportional to the FoM. Thus, it is projected that higher quality, better-oriented KNN would begin to close the gap in power density between PZT- and KNN-based harvesters. To further increase the efficiency of the design, one can imagine coupling the compliant design with an in-plane wedge shaped beam design. The in-plane wedge shape increases the bending stiffness at the beam clamping area, which would be useful in homogenizing the strain levels along the beam length.

SUPPLEMENTARY MATERIAL

See the supplementary material for additional structural characterization and additional baseline electrical properties of KNN films. Output voltage vs frequency and acceleration characterization for PZT- and KNN-based harvesters are also reported.

ACKNOWLEDGMENTS

DATA AVAILABILITY

The data that support the findings of this study are available within the article and its supplementary material.

REFERENCES

[1]European Commission, see https://ec.europa.eu/digital-single-market/en/internet-of-things for "The Internet of Things" (2020).

[2]L. M. Miller, E. Halvorsen, T. Dong, and P. K. Wright, "Modeling and experimental verification of low-frequency MEMS energy harvesting from ambient vibrations," J. Micromech. Microeng. **21**, 045029 (2011).

[3]S. Priya, "Advances in energy harvesting using low profile piezoelectric transducers," J. Electroceram. **19**, 167–184 (2007).

[4]W. Wang, T. Yang, X. Chen, and X. Yao, "Vibration energy harvesting using a piezoelectric circular diaphragm array," IEEE Trans. Ultrason., Ferroelectr., Freq. Control **59**, 2022–2026 (2012).

[5]S. Roundy and P. K. Wright, "A piezoelectric vibration-based generator for wireless electronics," Smart Mater. Struct. **13**, 1131–1142 (2004).

[6]Y. B. Jeon, R. Sood, J.-h. Jeong, and S.-G. Kim, "MEMS power generator with transverse mode thin film PZT," Sens. Actuators, A **122**, 16–22 (2005).

[7]D. Shen, J.-H. Park, J. H. Noh, S.-Y. Choe, S.-H. Kim, H. C. Wikle III, and D.-J. Kim, "Micromachined PZT cantilever based on SOI structure for low frequency vibration energy harvesting," Sens. Actuators, A **154**, 103–108 (2009).

[8]S. S. Won, H. Seo, M. Kawahara, S. Glinsek, J. Lee, Y. Kim, C. K. Jeong, A. I. Kingon, and S.-H. Kim, "Flexible vibrational energy harvesting device using strain-engineered perovskite piezoelectric thin films," Nano Energy **55**, 182–192 (2019).

[9]N. Godard, L. Allirol, A. Latour, S. Glinsek, M. Gerard, J. Polesel, F. D. Dos Santos, and E. Defay, "1-mW vibration energy harvester based on a cantilever with printed polymer multilayers," Cell Rep. Phys. Sci. **1**, 100068 (2020).

[10]K. Coleman, J. Walker, T. Beechem, and S. Trolier-McKinstry, "Effect of stresses on the dielectric and piezoelectric properties of Pb(Zr$_{0.52}$Ti$_{0.48}$)O$_3$ thin films," J. Appl. Phys. **126**, 034101 (2019).

[11]X. Ma, A. Wilson, C. D. Rahn, and S. Trolier-McKinstry, "Efficient energy harvesting using piezoelectric compliant mechanisms: Theory and experiment," J. Vib. Acoust. **138**(2), 021005 (2016).

[12]S. Roundy, E. S. Leland, J. Baker, E. Carleton, E. Reilly, E. Lai, B. Otis, J. M. Rabaey, P. K. Wright, and V. Sundararajan, in *Improving Power Output for Vibration-Based Energy Scavengers* (IEEE CS and IEEE ComSoc, 2005), pp. 1536–1268.

[13]B. Ahmed Seddik, "Systèmes de récupération de l'énergie vibratoire large bande," Doctoral dissertation (Université de Grenoble Alpes, 2012).

[14]H. G. Yeo, X. Ma, C. Rahn, and S. Trolier-McKinstry, "Efficient piezoelectric energy harvesters utilizing (001) textured bimorph PZT films on flexible metal foils," Adv. Funct. Mater. **26**(32), 5940–5946 (2016).

[15]"Commission Regulation (EU) 2015/628 of 22 April 2015 amending Annex XVII to Regulation (EC) No 1907/2006 of the European Parliament and of the Council on the Registration, Evaluation, Authorization and Restriction of Chemicals (REACH) as Regards Lead and Its Compounds" (2015).

[16]"Directive 2012/19/EU of the European Parliament and of The Council of 4 July 2012 on Waste Electrical and Electronic Equipment (WEEE)" (2012).

[17]"EU-Directive 2002/95/EC: Restriction of the Use of Certain Hazardous Substances in Electrical and Electronic Equipment (RoHS)" (2003).

[18]C.-H. Hong, H.-P. Kim, B.-Y. Choi, H.-S. Han, J. S. Son, C. W. Ahn, and W. Jo, "Lead-free piezoceramics—Where to move on?," J. Materiomics **2**, 1–24 (2016).

[19]K.-I. Park, J. H. Son, G. T. Hwang, C. K. Jeong, J. Ryu, M. Koo, I. Choi, S. H. Lee, M. Byun, Z. L. Wang, and K. J. Lee, "Highly-efficient, flexible piezoelectric PZT thin film nanogenerator on plastic substrates," Adv. Mater. **26**, 2514 (2014).

[20]C. K. Jeong, "Toward bio-implantable and biocompatible flexible energy harvesters using piezoelectric ceramic materials," MRS Commun. **10**, 365–378 (2020).

[21]K. Shibata, K. Suenaga, K. Watanabe, F. Horikiri, A. Nomoto, and T. Mishima, "Improvement of piezoelectric properties of (K,Na)NbO$_3$ films deposited by sputtering," Jpn. J. Appl. Phys. **50**, 041503 (2011).

[22]S. Park, M. Peddigari, J. H. Kim, E. Kim, G.-T. Hwang, J.-W. Kim, C.-W. Ahn, J.-J. Choi, B.-D. Hahn, J.-H. Choi, W.-H. Yoon, D.-S. Park, K.-I. Park, C. K. Jeong, J. W. Lee, and Y. Min, "Selective phase control of dopant-free potassium sodium niobate perovskites in solution," Inorg. Chem. **59**, 3042 (2020).

[23]H. Wu, Y. Zhang, J. Wu, J. Wang, and S. J. Pennycook, "Microstructural origins of high piezoelectric performance: A pathway to practical lead-free materials," Adv. Funct. Mater. **29**, 1902911 (2019).

[24]C. K. Jeong, J. H. Han, H. Palneedi, H. Park, G.-T. Hwang, B. Joung, S.-G. Kim, H. J. Shin, I.-S. Kang, J. Ryu, and K. J. Lee, "Comprehensive biocompatibility of nontoxic and high-output flexible energy harvester using lead-free piezoceramic thin film," APL Mater. **5**, 074102 (2017).

[25]T. R. Shrout and S. Zhang, "Lead-free piezoelectric ceramics: Alternatives for PZT?," J. Electroceram. **19**, 185 (2007).

[26]B. Jaffe, W. R. Cook, Jr., and H. Jaffe, *Piezoelectric Ceramics* (Academic Press, London, 1971).

[27]C. W. Ahn, S. Y. Lee, H. J. Lee, A. Ullah, J. S. Bae, E. D. Jeong, J. S. Choi, B. H. Park, and I. W. Kim, "The effect of K and Na excess on the ferroelectric and piezoelectric properties of KNN thin films," J. Phys. D **42**, 215304 (2009).

[28]A. Safari and E. K. Akdogan, *Piezoelectric and Acoustic Materials for Transducer Application* (Springer US, 2008).

[29]H. J. Seog, A. Ullah, and C. W. Ahn, "Recent progress in KNN Pb-free thin films," J. Korean Phys. Soc. **72**, 1467–1483 (2018).

[30]V. Kovacova, J. I. Yang, L. Jacques, S. W. Ko, W. Zhu, and S. Trolier-McKinstry, "Comparative solution synthesis of Mn doped (Na,K) NbO$_3$ thin films," Chem. Eur. J. **26**, 9356–9364 (2020).

[31]M. Zheng, Y. Hou, X. Yan, L. Zhang, and M. Zhu, "A highly dense structure boosts energy harvesting and cycling reliabilities of a high-performance lead-free energy harvester," J. Mater. Chem. C **5**, 7862–7870 (2017).

[32]S. S. Won, J. Lee, V. Venugopal, D. J. Kim, J. Lee, I. W. Kim, A. I. Kingon, and S.-H. Kim, "Pb free Mn doped KNN piezo thin films for MEMS based vibrational energy harvester applications," Appl. Phys. Lett. **108**, 232908 (2016).

[33]I. Kanno, T. Ichoda, K. Adachi, H. Kotera, K. Shibata, and T. Mishima, "Power-generation performance of lead-free (K,Na)NbO$_3$ piezoelectric thin-film energy harvesters," Sens. Actuators, A **179**, 132–136 (2012).

[34]B.-Y. Kim, I.-T. Seo, Y.-S. Lee, J.-S. Kim, S. Nahm, C.-Y. Kang, S.-J. Yoon, J.-H. Paik, and Y.-H. Jeon, "High-performance (Na$_{0.5}$K$_{0.5}$)NbO$_3$ thin film piezoelectric energy harvester," J. Am. Ceram. Soc. **98**, 119–124 (2015).

[35]Y. Tsujiura, E. Suwa, F. Kurokawa, H. Hida, K. Suenaga, K. Shibata, and I. Kanno, "Lead-free piezoelectric MEMS energy harvesting of (K,Na) NbO$_3$ thin films on strainless steel cantilevers," Jpn. J. Appl. Phys. **52**, 09KD13 (2013).

[36]H. G. Yeo, "Mechanical energy harvesting utilizing {001} textured PZT films on flexible metal foils," Doctoral dissertation (The Pennsylvania State University, 2017).

[37]J. F. Shepard, Jr., P. J. Moses, and S. Trolier-McKinstry, "The wafer flexure technique for the determination of the transverse piezoelectric coefficient (d_{31}) of PZT thin films," Sens. Actuators, A Phys. **71**(1–2), 133–138 (1998).

[38]X Ma, "Dynamics and control of energy harvesting devices," Doctoral dissertation (The Pennsylvania State University, 2017).

[39]B. Dubus, J. C. Debus, J. N. Decarpigny, and D. Boucher, "Analysis of mechanical limitations of high power piezoelectric transducers using finite element modelling," Ultrasonics **29**(3), 201–207 (1991).

[40]A. D. Handoko and K. L. G. Goh, "Hydrothermal synthesis of sodium potassium niobate solid solutions at 200 °C," Green Chem. **12**, 680 (2010).

[41]R. W. Schwartz, T. J. Boyle, S. J. Lockwood, M. B. Sinclair, D. Dimos, and C. D. Buchheit, "Sol-gel processing of PZT thin films: A review of the state-of-the-art and process optimization strategies," Integr. Ferroelectr. **7**(1–4), 259–277 (1995).

[42]F. Calame and P. Muralt, "Growth and properties of gradient free sol-gel lead zirconate titanate thin films," Appl. Phys. Lett. **90**, 062907 (2007).

[43]A. Kupec, B. Malic, J. Tellier, E. Tchernychova, S. Glinsek, and M. Kosec, "Lead-free ferroelectric potassium sodium niobate thin films from solution: Composition and structure," J. Am. Ceram. Soc. **95**(2), 515–523 (2012).

[44]A. Kupec, H. Ursic, R. C. Frunza, E. Tchernychova, and B. Malic, "Microstructure dependant leakage current properties of solution-derived (K$_{0.5}$Na$_{0.5}$)NbO$_3$ thin films," J. Eur. Ceram. Soc. **35**(13), 3507–3511 (2015).

[45]F. Griggio and S. Trolier-McKinstry, "Grain size dependence of properties in lead nickel niobate-lead zirconate titanate films," J. Appl. Phys. **107**, 024105 (2010).

[46]X. Du, J. Zheng, U. Belegundu, and K. Uchino, "Crystal orientation dependence of piezoelectric properties of lead zirconate titanate near the morphotropic phase boundary," Appl. Phys. Lett. **72**(19), 2421 (1998).

[47]P. Muralt, "Recent progress in materials issues for piezoelectric MEMS," J. Am. Ceram. Soc. **91**, 1385 (2008).

[48]P. Li, J. Zhai, B. Shen, S. Zhang, X. Li, F. Zhu, and X. Zhang, "Ultrahigh piezoelectric properties in textured (K,Na)NbO$_3$-based lead-free ceramics," Adv. Mater. **30**, 8 (2018).